JGR Solid Earth

RESEARCH ARTICLE
10.1029/2022JB024288

Stability of a Mixed-Valence Hydrous Iron-Rich Oxide: Implications for Water Storage and Dynamics in the Deep Lower Mantle

Lu Liu[1,2], Ziqiang Yang[1], Hongsheng Yuan[1], Yue Meng[3], Nico Giordano[4], Junliang Sun[5], Xueyan Du[1], Philip Dalladay-Simpson[1], Junyue Wang[1], and Li Zhang[1]

[1]Center for High Pressure Science and Technology Advanced Research, Shanghai, China, [2]School of Physical Sciences, University of Science and Technology of China, Hefei, China, [3]HPCAT, X-Ray Science Division, Argonne National Laboratory, Lemont, IL, USA, [4]Deutsches Elektronen-Synchrotron (DESY), Petra III, Hamburg, Germany, [5]College of Chemistry and Molecular Engineering, Peking University, Beijing, China

Key Points:

- An iron-rich hexagonal hydrous phase is stable at 1,900–2,400 km depth
- Chemical composition of the hydrous phase was found to vary with bulk composition and with pressure
- The iron-rich hydrous phase could be major water storage in a pyrolitic deep lower mantle and decompose in upwelling plumes

Supporting Information:

Supporting Information may be found in the online version of this article.

Correspondence to:

L. Zhang,
zhangli@hpstar.ac.cn

Citation:

Liu, L., Yang, Z., Yuan, H., Meng, Y., Giordano, N., Sun, J., et al. (2022). Stability of a mixed-valence hydrous iron-rich oxide: Implications for water storage and dynamics in the deep lower mantle. *Journal of Geophysical Research: Solid Earth*, *127*, e2022JB024288. https://doi.org/10.1029/2022JB024288

Received 25 FEB 2022
Accepted 4 MAY 2022

Abstract Incorporation of water into mantle compositions can have significant effects on the phase relations in the systems. In this study, we synthesized an iron-rich hexagonal hydrous phase (referred to as "HH1-phase") under the high pressure-temperature (*P-T*) conditions of the deep lower mantle and determined the crystal structure of the HH1-phase at 79 GPa using the multigrain crystallography method. The chemical formula obtained was $Fe_{12.76}O_{18}H_x$ ($x \sim 4.5$) in the Fe-O-H system. To demonstrate the role of HH1-phase for water storage in multicomponent systems relevant to mantle compositions, we investigated the stability of HH1-phase in both MgO-rich pyrolitic and SiO_2-rich basaltic compositions. Our results indicate that the HH1-phase serves as major water storage in a pyrolitic composition, whereas the Al-rich $CaCl_2$-type δ-phase and SiO_2 phase are major water storage phases in a SiO_2-rich basaltic composition. Incorporation of considerable amounts of SiO_2, MgO, and Al_2O_3 into the HH1-phase expands its stability field from 98 GPa in the Fe-Al-O-H system to at least 108 GPa (corresponding to ~2,400 km depth) in the Mg-Si-Al-Fe-O-H system. Plumes of hot upwelling rock rooted at the base of the lower mantle have been proposed as a possible origin of hotspot volcanoes. The hydrous Fe-rich HH1-phase, if included into the material of upwelling plumes, will decompose on its rising to the upper part of the lower mantle and release water. Our results should provide constraints on water storage in the deep lower mantle and have implications for deep mantle dynamics.

Plain Language Summary Incorporation of water into mantle compositions can have significant effects on the phase relations in the system. In this study, we conducted experiments under high pressure-temperature (*P-T*) conditions of the deep lower mantle in a laser-heated diamond anvil cell. We synthesized an iron-rich hexagonal hydrous phase (referred to as "HH1-phase") as $Fe_{12.76}O_{18}H_x$ ($x \sim 4.5$) in the Fe-O-H system and confirmed the stability of HH1-phase in multicomponent mantle systems under high *P-T* conditions corresponding to the depth of 1,900–2,400 km. Our results indicate that the HH1-phase could play a major role as water storage in a pyrolitic deep lower mantle. Plumes of hot upwelling rock rooted at the base of the lower mantle have been proposed as a possible origin of hotspot volcanoes. The hydrous Fe-rich HH1-phase, if included into the material of upwelling plumes, will decompose on its rising to the upper part of the lower mantle and release water. Our results should provide constraints on water storage in the deep lower mantle and have implications for deep mantle dynamics.

1. Introduction

There is a general consensus that the Earth's upper mantle is pyrolitic in composition, but whether the composition of the lower mantle is pyrolitic remains debated (Irifune et al., 2010; Ricolleau et al., 2009). Seismic data reveal two large low-shear-wave-velocity provinces (LLSVPs) in the deep lower mantle (Su et al., 1994) and compositional anomalies are required to explain the seismic observations (Ni et al., 2002; Trampert et al., 2004). Both accumulation of mid-ocean-ridge basalt (MORB) material (Nakagawa et al., 2010) and survival of primitive reservoirs of dense material (Deschamps et al., 2012; Labrosse et al., 2007) have been proposed to explain the origin of the LLSVPs. The correlation of hotspot locations with the LLSVPs implies a deep-rooted origin for the surface observations (Thorne et al., 2004) and the seismic imaging data further provide evidence for upwelling plumes rooted at the base of the lower mantle (French & Romanowicz, 2015). On the other hand, water, even in

extremely small amounts, plays a critical role in the mantle dynamics (Maruyama et al., 2007). The ocean-island basalts with a lower mantle origin appear to have the highest water content (Dixon et al., 2002). The high water content observed in komatiites from mantle plumes and picrites from LIPs (Liu et al., 2017; Sobolev et al., 2016) further indicate deep mantle water reservoirs. Water can also have a significant effect on the viscosity that is an important parameter in mantle plume dynamics (Jellinek & Manga, 2002). Thus, constraining water storage in multicomponent systems relevant to the deep lower mantle is of fundamental importance for understanding the effects of water on composition and dynamics of the deep lower mantle.

Previous studies have demonstrated that adding water into the multicomponent systems can have significant effects on phase relations in the deep lower mantle (Ohira et al., 2014; Walter et al., 2015; Yuan et al., 2019). The water solubility in bridgmanite (Bdg), the dominant mineral in the lower mantle, remains debated with estimated solubility ranging from tens to thousands ppm (Fu et al., 2019; Litasov et al., 2003) and the water solubility in Bdg phase can be greatly affected by mantle compositions (Litasov et al., 2003). Besides nominally anhydrous minerals, the dense hydrous magnesium silicates (DHMS phases), such as phase D [$MgSi_2H_2O_6$] and phase H [$MgSiO_4H_2$], can transport and store water in the lower mantle (Nishi et al., 2014; Pamato et al., 2015). Chemical compositions of the hydrous phases change with mantle compositions and high pressure-temperature (*P-T*) conditions (Ohira et al., 2014; Pamato et al., 2015; Walter et al., 2015; Yuan et al., 2019). For example, the thermal stability of phase H is greatly enhanced by incorporation of alumina under high *P-T* conditions (Ohira et al., 2014; Pamato et al., 2015; Sano et al., 2008; Walter et al., 2015). The phase H [$MgSiO_4H_2$], δ-AlOOH, and ε-FeOOH all adopt a $CaCl_2$-like structure and can form solid solutions owing to their structural similarities (Ohira et al., 2014; Sano et al., 2008; Yuan et al., 2019). The ε-FeOOH is stable above 5 GPa (Gleason et al., 2013) until it transforms to the pyrite-structured $FeOOH_x$ ($0 < x \leq 1$) (referred to as "py-phase") above 85 GPa and 1600 K (Hu et al., 2016; Nishi et al., 2017). For simplicity, we refer to all solid solutions of phase H, δ-AlOOH, and ε-FeOOH as the $CaCl_2$-type δ-phase, which is considered as a potential water reservoir in the lower mantle (Ohira et al., 2014; Walter et al., 2015; Yuan et al., 2019). Several separate studies recently reported a previously unknown hexagonal phase in the hydrous systems under the *P-T* conditions of the lower mantle but the results showed fundamental differences in the O/Fe ratio and hydrogen content of the phase despite the similarities in the reported unit-cell parameters (Chen et al., 2020; Koemets et al., 2021; Liu et al., 2020).

There have been few phase equilibrium data in hydrous multicomponent systems relevant to the lower mantle mainly due to difficulties in characterization of multiphase assemblages at extremely high *P-T* conditions. The proposed composition models for the LLSVPs range from SiO_2-rich MORB composition to Fe-enriched primitive material close to a pyrolitic composition (Deschamps et al., 2012). To understand the effects of mantle composition on water storage in the deep lower mantle, in this study, we conducted a series of experiments in the Fe-O-H, Fe-Al-O-H, Mg-Fe-O-H, Mg-Fe-Si-O-H, and Fe-Al-Mg-Si-O-H systems using a laser-heated diamond anvil cell (LH-DAC) under high *P-T* conditions (Table 1). We determined chemical composition and crystal structure of submicron-sized individual grains in a multiphase assemblage combining *in-situ* multigrain X-ray diffraction (XRD) with *ex-situ* transmission electron microscopy (TEM) analysis (Zhang et al., 2016, 2019).

2. Materials and Methods

The starting materials $Al_{0.2}Fe_{0.8}(OH)_3$, $Al_{0.8}Fe_{0.2}(OH)_3$, $Fe(OH)_3$, $FeO + H_2O$, $(Mg_{0.8}Fe_{0.2})O + H_2O$, $(Mg_{0.9}Fe_{0.1})_2SiO_4 + H_2O$, and MgO-Fe_2O_3-SiO_2-Al_2O_3-H_2O gels were used in this study (Text S1 in Supporting Information S1) and the details of preparation and characterization of the gel samples were described elsewhere (Yuan et al., 2019). Composition and homogeneity of the starting materials were confirmed by a scanning electron microscope coupled with EDS analysis (Figure S1 in Supporting Information S1). LH-DAC experiments were performed between 70 and 108 GPa and 1600–2400 K (Table 1). In most runs, Ne was used as pressure medium and its equation of state was used to calibrate pressures (Fei et al., 2007). All the sample pressures were measured after *T* quench unless noted otherwise. The thermal pressures are estimated as $Pth = (T-300)*0.0062$ (GPa) from a previous study under similar *P-T* conditions (Yuan et al., 2019). In other runs water or hydrous silica was used as pressure medium and pressures were calibrated by the Raman shift of diamond (Akahama & Kawamura, 2007) or unit-cell parameters of Au or Ne (Fei et al., 2007).

The *in-situ* XRD measurements coupled with laser-heating were conducted at High Pressure Collaborative Access Team (HPCAT), 16-ID-B beamline of Advanced Photon Source (APS), Argonne National Laboratory (Argonne,

Table 1
Experimental Conditions and Results

Run#	*P-T* conditions	Heating duration	Phase assemblage
$Al_{0.2}Fe_{0.8}(OH)_3$			
Sa083[a]	79 GPa, 1600 K	3 min	δ
	79 GPa, 1800 K	2 min	HH1, δ
	79 GPa, 2100 K	13 min	HH1, δ
	79 GPa, quench from 2100 K		HH1, δ
Sb211	70 GPa, quench from 2100 K	10 min	HH1, δ
Sb343a[c]	80 GPa, quench from 2100 K	10 min	HH1, δ
Sa069	86 GPa, quench from 2300 K	10 min	HH1, δ, py
$Al_{0.8}Fe_{0.2}(OH)_3$			
Sb307a	80 GPa, quench from 2000 K	10 min	HH1, δ
$Fe(OH)_3$			
Sb343b	78 GPa, quench from 2200 K	10 min	HH1, ε
$FeO + H_2O$			
Sb390	80 GPa, quench from 2100 K	10 min	HH1
$Fe_2O_3 + H_2O$			
Sb347[b]	74 GPa, quench from 2400K	10 min	HH1, pPv-Fe2O3
54.8 mol % SiO_2-12.8 mol% Al_2O_3-24.9 mol% MgO-7.5 mol% Fe_2O_3 ~7 wt.% H_2O (MASFH8)			
Sb397[c]	74 GPa, quench from 2000 K	10 min	HH1, δ, Bdg, Nt-SiO_2
65.6 mol% SiO_2-12.3 mol% Al_2O_3-16.4 mol% MgO-5.7 mol% Fe_2O_3 ~7wt.% H_2O (MASFH6)			
Sb307b[c]	96 GPa, quench from 2300K	10 min	HH1, δ, Bdg, $CaCl_2$-SiO_2
40 mol% $MgSiO_3$-30 mol% Al_2O_3-30 mol% Fe_2O_3 ~7wt.% H_2O (MASFH30)			
Sb335[c]	79 GPa, quench from 2000 K	10 min	HH1, δ, Bdg, pPv-Fe_2O_3
$Mg_{0.8}Fe_{0.2}O + H_2O$ (Fp20 + H_2O)			
Sb430	79 GPa, quench from 2000 K	30 min	HH1, Fp
$(Mg_{0.9}Fe_{0.1})_2SiO_4 + H_2O$ (olivine + H_2O)			
Sb329	77 GPa, quench from 2000 K	30 min	HH1, Fp, Bdg

Note. Here δ represents the $CaCl_2$-type hydrous phases. The unit-cell parameters of individual phases are provided in Table S1 in Supporting Information S1.

[a]The pressure of run# Sa083 was calibrated by the EOS of Ne after quenched from 2100K. [b]The starting material of run# Sb347 was Fe_2O_3 sandwiched between two layers of hydrous SiO_2. [c]Chemical analysis was performed on the recovered samples in a TEM and the compositions of HH1-phase are listed in Table 3.

IL) (Run# Sa083). Each sample was compressed to a target pressure and then heated using a double-sided heating system equipped with Ytterbium fiber lasers. The measured temperature uncertainties were within ±150 K. The XRD measurements after *ex-situ* laser-heating were conducted at 15U beamline of Shanghai Synchrotron Radiation Facility (SSRF) and the P02.2 beamline of the PETRA III synchrotron at Deutsches Elektronen Synchrotron. The thin-sections of the recovered samples were prepared by focused ion beam. Chemical analysis of recovered samples was performed by TEM operating at 200 kV equipped with an EDS system. Further details about the experiments and data analysis can be found in Text S2 and S3 in Supporting Information S1.

The sample (Run# Sa083) was aligned to the rotation center and a rotation data set was collected by rotating the DAC from −26.0 to 25.0° in small incremental steps of 0.25°. The X-ray wavelength was 0.3445 Å and the exposure time was 5 s/frame. The rotation data set was processed using the FABLE package (Sørensen et al., 2012) and the GrainSpotter software within the package was used to index individual grains for each phase in the assemblage (Schmidt, 2014). The X-ray Detector Software package was used for processing the single-crystal diffraction data (Kabsch, 2010).

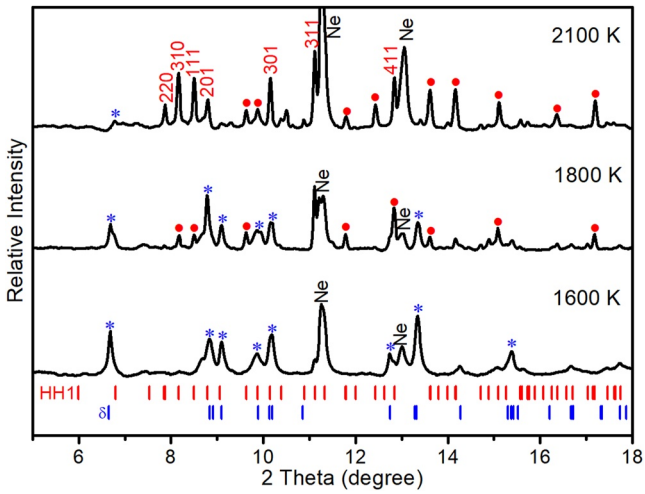

Figure 1. *In-situ* X-ray diffraction (XRD) observation of decomposition of δ-(Fe, Al)OOH into the HH1-phase and Al-rich δ-phase at 79 GPa and 1600–2100 K. The starting material was $(Al_{0.2}Fe_{0.8})(OH)_3$ (Run# Sa083). A pure δ-phase was synthesized at 1600 K. The HH1-phase appeared at 1800 K and became dominant at the expense of the δ-phase at 2100 K with $a = 10.071(4)$ Å, $c = 2.622(1)$ Å and $V = 230.3(2)$ Å^3. The peaks from the HH1-phase and δ-phase are marked by red dots and blue asterisks, respectively. The calculated peak positions are indicated by small ticks. The peaks in the high *d*-spacing region were labeled with the Miller indices (hkl) in the XRD pattern collected at 2100 K and used for determination of the lattice parameters. The X-ray wavelength was 0.3445 Å.

3. Results and Discussions

3.1. Synthesis and Characterization of the HH1-Phase

First, the starting material $Al_{0.2}Fe_{0.8}(OH)_3$ was loaded in a Ne medium (Run# Sa083, Table 1). Only the diffraction peaks of the $CaCl_2$-type δ-phase appeared when the sample was heated at 1600 K for 3 min at 79 GPa. After the sample was heated at an elevated temperature of 1800 K for another 2 min, a new set of peaks appeared in addition to those of the δ-phase. We observed a gradual growth of the new phase at the expense of δ-phase and the new phase became dominant after heating at 2100 K for another 13 min. The phase was indexed with a hexagonal unit-cell of $a = 10.0230(4)$ Å and $c = 2.6063(2)$ Å at 79 GPa and after *T* quench, as shown in Figure 1. The results indicate that the Fe-rich δ-phase (Fe,Al)OOH is unstable under high *P-T* conditions of the deep lower mantle (Katsura et al., 2010).

The hexagonal phase was reproduced in another two separate runs coexisting with the $CaCl_2$-type δ-phase using the same starting material (Run# Sb211, Sb343a, Figure S2 in Supporting Information S1). To measure the chemical composition, the sample synthesized at 80 GPa and 2100 K (Run Sb#343a) was recovered to ambient conditions for chemical analysis by TEM. We found that the Al content (~1.5 at%) in the Fe-rich hexagonal phase was negligible and the Fe content in the δ-phase was determined at roughly 13 at% using energy dispersive X-ray spectroscopy (EDS) (Figure S3 in Supporting Information S1). The hexagonal phase was also synthesized in an Al-free system with the starting material $Fe(OH)_3$ (equivalent to $Fe_2O_3 + 3H_2O$) at 78 GPa and 2000 K (Run# Sb343b). A nearly pure hexagonal phase was obtained with $a = 10.014(2)$ Å and $c = 2.6158(6)$ Å. The sample was further heated at 2200 K for another 10 min to test its thermal stability and the phase remained stable only with better crystallization (Figure 2a).

EDS does not provide a reliable quantitative analysis for light elements, such as oxygen content in the phase. In addition, unreacted water from the starting material could also interfere with the measurement of oxygen content in the run products. Instead, we use high quality *in-situ* single-crystal data to extract reliable chemical composition of the phase (i.e., O/Fe ratio). The spottiness of the XRD pattern (Run# Sa083) allowed *in-situ* multigrain indexation and single-crystal structure determination. A representative spotty XRD pattern of the HH1-phase in Ne medium is shown in Figure S4 in Supporting Information S1. We indexed 28 individual grains belonging to the hexagonal phase, selected three of the grains with maximum number of reflections for the structure analysis. In total, 774 reflections were merged from the three grains to achieve a completeness of 94%. A reasonable $R1 = 5.59\%$ was obtained for all data. The reflections indexed from powder XRD and the refined atomic coordinates from single-crystal structure data are listed in Table 2. The structure and refinement details are provided in Dataset S1.

The chemical formula of the hexagonal phase was obtained as $Fe_{12.76}O_{18}$ and it is difficult to quantitatively resolve the hydrogen content. Assuming a linear relationship between the density of iron oxides and the O/Fe ratio at 80 GPa (Koemets et al., 2021), the measured density assuming a composition of $Fe_{12.76}O_{18}$ is ~3.5% smaller than the density derived from the linear relationship, indicating a volume expansion induced by incorporation of hydrogen (Figure 3). The hydrogen content can be estimated based on the equations of state of hcp-Fe (Fei et al., 2016) and FeH (Pépin et al., 2014), which was obtained as 1.61 Å^3 per hydrogen atom at 80 GPa. The volume expansion was calculated as 0.62 Å^3 per Fe atom for the hexagonal phase (Sb#343b) and therefore the hydrogen content was estimated as $x \sim 4.9$ in $Fe_{12.76}O_{18}H_x$. Note that this stoichiometry almost matches the distribution of ferric and ferrous Fe occupying the octahedral and prismatic sites, respectively, and we then use $x \sim 4.5$ as $Fe_{12.76}O_{18}H_{4.5}$. Synchrotron Mössbauer spectroscopy is used to measure the electronic structure of iron under high pressure, but *in-situ* quantitative characterization of iron valence state in a mixed-valence iron-bearing

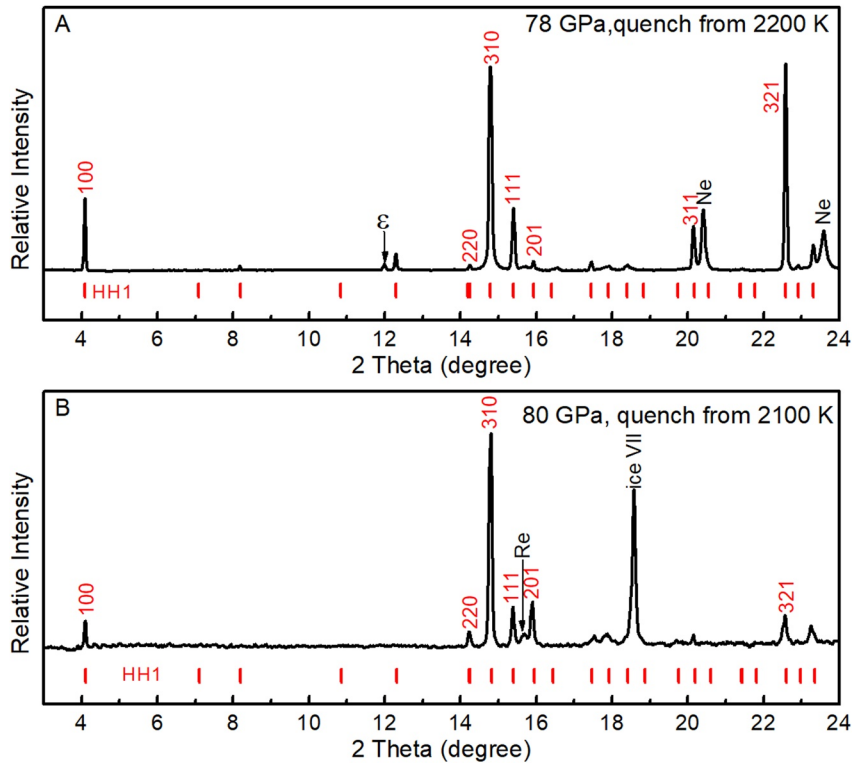

Figure 2. Synthesis of the HH1-phase in the Fe_2O_3-H_2O and FeO-H_2O systems, respectively. (a) The HH1-phase was synthesized using the starting material of $Fe(OH)_3$ and remained stable after heating at 2200 K for 10 min (Run# Sb343b). (b) The HH1-phase coexisting with ice-VII at 80 GPa and *T* quench from 2100 K using the starting material of FeO + H_2O (Run# Sb390). The X-ray wavelength was 0.6199 Å.

mineral at the deep lower mantle pressures has remained as a great challenge (Bengtson et al., 2009). Note that neither the exact hydrogen content nor the actual site distribution of Fe^{2+} and Fe^{3+} can be directly measured in our study, but the hydrous nature and mixed valence state of Fe in the phase is confirmed. This iron-rich hexagonal hydrous phase is referred to as the "HH1-phase" hereafter.

To understand the formation mechanism of the HH1-phase, we conducted another experiment on FeO loaded in a H_2O medium. The amount of H_2O in the sample chamber was oversaturated for the reaction. The sample was compressed to 80 GPa and then heated at 2100 K for 10 min (Run# Sb390). The HH1-phase was again obtained coexisting with ice-VII (Figure 2b), suggesting that the formation of HH1-phase is independent on the iron valence state in starting materials. An XRD pattern was collected immediately after the sample was decompressed to ambient conditions (Figure S5 in Supporting Information S1). Although the diffraction intensities of HH1-phase were weak, we were still able to determine the unit-cell parameters as $a = 11.437(3)$ Å, $c = 2.929(1)$ Å, and $V = 331.8(2)$ Å^3. We then observed a gradual disappearance of the diffraction signal with time, implying instability of the structure under ambient conditions.

The HH1-phase $Fe_{12.76}O_{18}H_{4.5}$ obtained in this study has a unit-cell similar to those of the $Fe_{6.32}O_9$ phase (Koemets et al., 2021), the η-phase $Fe_{12}O_{18+x/2}H_x$ ($x \approx 2$) where all iron in ferric (Chen et al., 2020), and the OE-phase $(Mg,Fe)_2O_{3+\delta}$ ($0 < \delta < 1$) with an O/Fe ratio >1.5 (Liu et al., 2020), but these reported chemical formulas show fundamental differences in the O/Fe ratio and hydrogen contents. The main discrepancy lies in whether the hexagonal channels formed by the chains of FeO_6 octahedra are filled with partially occupied Fe or fully occupied O. High quality structure data allow us to distinguish the differences between these two models due to the nonlinear relations of atomic scattering against the atomic numbers. If Fe_{00} position is filled with O, we obtained R_1/wR_2 (all data) = 0.072/0.213. In our structure model where the Fe_{00} position is filled with Fe of 0.381(10) occupancy, we obtained R_1/wR_2 (all data) = 0.0559/0.1335. The improvement of the refinement is significant. The structure model of HH1-phase obtained in our study is in good agreement with that of $Fe_{6.32}O_9$

Table 2
(A) Indexed Powder X-Ray Diffraction Peaks of the HH1-Phase at 79 GPa and After T Quench From 2100 K (Run# Sa083)

A	*hkl*	2θ-obs, °	*d*-obs, Å	*d*-calc, Å	*d*-diff, Å
	100	2.277	8.6692	8.6789	−0.0097
	200	4.545	4.3440	4.3395	0.0046
	210	6.018	3.2814	3.2803	0.0011
	300	6.824	2.8942	2.8930	0.0012
	220[a]	7.897	2.5015	2.5054	−0.0039
	310[a]	8.196	2.4104	2.4071	0.0033
	111[a]	8.528	2.3167	2.3163	0.0004
	201[a]	8.833	2.2368	2.2379	−0.0011
	400	9.122	2.1661	2.1697	−0.0036
	211[a]	9.673	2.0430	2.0434	−0.0004
	301[a]	10.193	1.9390	1.9387	0.0003
	311[a]	11.170	1.7699	1.7701	−0.0002
	221	10.935	1.8078	1.8081	−0.0003
	330	11.834	1.6709	1.6703	0.0007
	321	12.487	1.5839	1.5835	0.0004
	411[a]	12.895	1.5339	1.5333	0.0007
B	Atom	S.O.F.	x/a	y/b	z/c
	Fe01		0.74451 (17)	0.05948 (16)	0.75
	Fe02		0.83694 (14)	0.38349 (13)	0.25
	Fe00	0.381 (10)	1.0	0	1.0
	O3		0.7161 (7)	0.2257 (7)	0.75
	O1		0.5949 (7)	−0.0103 (7)	0.25
	O2		0.7522 (8)	−0.1146 (8)	0.75

Note. The unit-cell parameters obtained were $a = 10.021(2)$ Å and $c = 2.6121(9)$ Å. The X-ray wavelength was 0.3445 Å. (B) The atomic parameters of the HH1-phase with the space group of P63/m.
[a]Strong peaks in the powder XRD patterns.

phase (Koemets et al., 2021). In the hollandite-like structures (Foo et al., 2006; Miura et al., 2000), Na or Ca cations (occupancies of 1/3 and 1/2, respectively) lie in the channels instead of O, similar to our structure model of the HH1-phase. In addition, Raman signal of O_2 was detected in the sample chamber where $Fe(OH)_3$ with all iron in ferric was used as the starting material (Run# Sb343b, Figure S6 in Supporting Information S1). A nearly pure HH1-phase was obtained (Figure 2a). The release of O_2 along with the formation of HH1-phase suggests reduction of Fe^{3+} under hydrous condition, confirming the mixed valence state of Fe in the HH1-phase. When the *P-T* conditions were increased to 86 GPa and 2300 K (~98 GPa after accounting for the thermal pressure), we observed the appearance of py-phase with peak intensities comparable to those of the coexisting HH1-phase (Run# Sa069, Figure S2 in Supporting Information S1). The pure py-phase was synthesized in the Fe-O-H system at 112 GP and 2080 K and 110 GPa and 2250 K, respectively (Mao et al., 2017). Another hexagonal hydrous phase (denoted as "HH-phase") was reported previously with unit-cell parameters of $a = 10.5803(6)$ Å, $c = 2.5897(3)$ Å, and $V = 251.06(3)$ Å^3 at 110 GPa (Zhang et al., 2018), in contrast to $a = 10.0230(4)$ Å, $c = 2.6063(2)$ Å, and $V = 226.75(2)$ at 79 GPa for the HH1-phase. Figure S7 in Supporting Information S1 shows a *P-T* diagram of the hexagonal phases obtained in the Fe-O-H and Fe-Al-O-H systems along with the suggested geotherms for both slab and normal mantle (Brown & Shankland, 1981; Kirby et al., 1996). The HH1-phase is a low-pressure phase relative to the py-phase and HH-phase. Future experiments are needed to determine the *P-T* boundaries for the phase transformations of these hydrous phases.

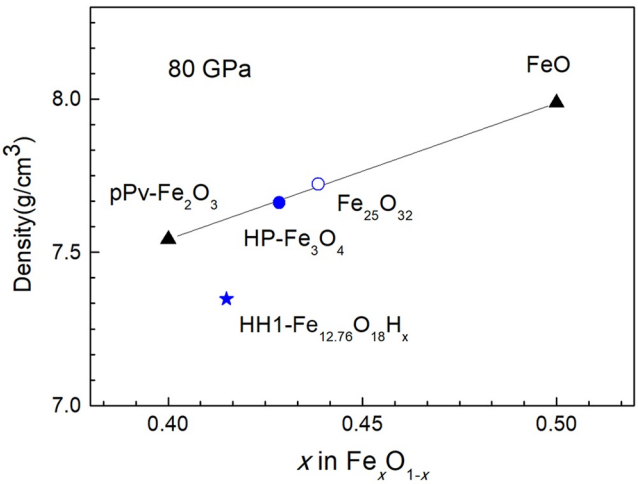

Figure 3. The density of iron oxides as a function of their chemical compositions. We assumed a linear relationship between the densities of 7.987 g/cm^3 for B1-FeO (Fischer et al., 2011) and 7.542 g/cm^3 for pPv-Fe_2O_3 (solid black triangles) at 80 GPa and room *T*. The density of pPv-Fe_2O_3 was derived from the unit-cell volumes listed in Table S1 in Supporting Information S1. The densities of 7.639 g/cm^3 for the HP-Fe_3O_4 ($V = 200.82$ Å^3) (Greenberg et al., 2017) and 7.722 g/cm^3 for the $Fe_{25}O_{32}$ phase ($V = 410.48(12)$ Å^3) (Bykova et al., 2016) were plotted, confirming the linear relationship. The density for the composition $Fe_{12.76}O_{18}$ is derived as 7.608 g/cm^3 based on the linear relationship, which is about 3.5% higher than that obtained from the measured unit-cell volume of $V = 226.2$ Å^3 (Run#Sb343a) assuming the composition $Fe_{12.76}O_{18}$ (solid blue star).

3.2. Water Storage in the Deep Lower Mantle

To demonstrate the stability of HH1-phase in multicomponent systems relevant to the lower mantle, we performed experiments in both MgO-rich and SiO_2-rich systems. First, crystals of natural olivine [$(Mg_{0.9}Fe_{0.1})_2SiO_4$] were ground into a fine powder and then mixed with 10 wt.% gold as the laser absorber. The sample was loaded in a H_2O medium, compressed to 77 GPa and then laser-heated for 30 min at 2000 K. Both XRD data at high-*P* and TEM results on the recovered sample confirm the coexistence of the HH1-phase with ferropericlase (Fp) and Bdg (Run# Sb329) (Figure 4a and Figure 5). Interestingly, the chemical analysis revealed that the HH1-phase contains about 4.9 at% Mg and 7.1 at% Si (Table 3). We performed another experiment on Fp-$(Mg_{0.8}Fe_{0.2})O$ loaded in a H_2O medium at 79 GPa and heated at 2000 K for 30 min (Run# Sb430). The proportion of HH1-phase is significant in the run products coexisting with Fp (Figure 4b) and the chemical analysis indicates only ~1.5 at% Mg in the HH1-phase (Table 3), indicating the formation of HH1-phase at the expense of FeO content in the Fp-phase. The combined results suggest that the presence of Si^{4+} enhances the solubility of Mg^{2+} in the HH1-phase. However, the proportion of HH1-phase is relatively low in the run products from the reaction of olivine $(Mg_{0.9}Fe_{0.1})_2SiO_4 + H_2O$ likely due to a kinetics effect in these reactions. The kinetics of reactions at lower mantle conditions can be largely controlled by the diffusion behavior of minerals. For instance, the Mg-Fe interdiffusion coefficients for Bdg are more than four orders of magnitude lower than those of Fp at lower mantle conditions (Holzapfel et al., 2005). Kinetics in water-mineral reactions at lower mantle conditions is a topic for future study.

We performed another three separate experiments in SiO_2-rich systems to explore differences in water storage between MgO-rich and SiO_2-rich compositions. The gel sample with a composition of 54.8 mol% SiO_2-12.8 mol% Al_2O_3-24.9 mol% MgO-7.5 mol% Fe_2O_3+ ~7wt% H_2O (MASFH8, details see the Text S1 in Supporting Information S1) was prepared to represent a simplified basalt composition. We used these starting materials with all iron in Fe^{3+} as we have demonstrated that the formation of HH1-phase is independent of the valence state of Fe in starting materials. The gel sample was loaded in a Ne medium, compressed to 74 GPa and heated at 2000 K for 10 min (Run# Sb397). As shown in Figure 6a, the diffraction peaks from multiple phases overlap heavily in the powder XRD pattern where several characteristic peaks of the HH1-phase were visible but weak in intensity. We applied the multigrain method (Zhang et al., 2019) and indexed multiple individual grains belonging to Bdg, HH1-phase, d-NiAs-type SiO_2, and $CaCl_2$-type δ-phase, respectively (Table S2 in Supporting Information S1). The d-NiAs-type SiO_2 was stable in a narrow temperature range of 1000–1300 K at 30–60 GPa in the anhydrous system (Prakapenka et al., 2004), but it was stabilized at 1600–1700 K above 60 GPa by H_2O solubility into the phase (Nisr et al., 2020). The HH1-phase comprises only ~1.5 wt.% of the assemblage based on the mass balance calculations. In another experiment on a composition containing a larger proportion of SiO_2 (MASFH6, Run# Sb307b), the HH1-phase was again obtained coexisting with $CaCl_2$-type SiO_2, $CaCl_2$-type δ-phase, and Bdg at 96 GPa (~108 GPa after accounting for the thermal pressure) and 2300 K (Figure 6b). The chemical compositions of the HH1-phase are summarized in Table 3. In contrast to only ~2 at% Al in the HH1-phase at 74–78 GPa, the HH1-phase contains ~11 at.% Al at 108 GPa and 2300 K. The volumes of the HH1-phase are plotted as a function of pressure (Figure S8 in Supporting Information S1). Importantly, the chemical composition of HH1-phase was found to vary with bulk composition and with pressure (Table 3), incorporating considerable amounts of SiO_2, MgO, and Al_2O_3 into the HH1-phase. As a result, the stability field of the HH1-phase was extended from 98 GPa in Fe-Al-O-H system (Run# Sa069) to at least 108 GPa in the Mg-Si-Al-Fe-O-H system (Run# Sb307b), corresponding to a depth range of 1900–2400 km.

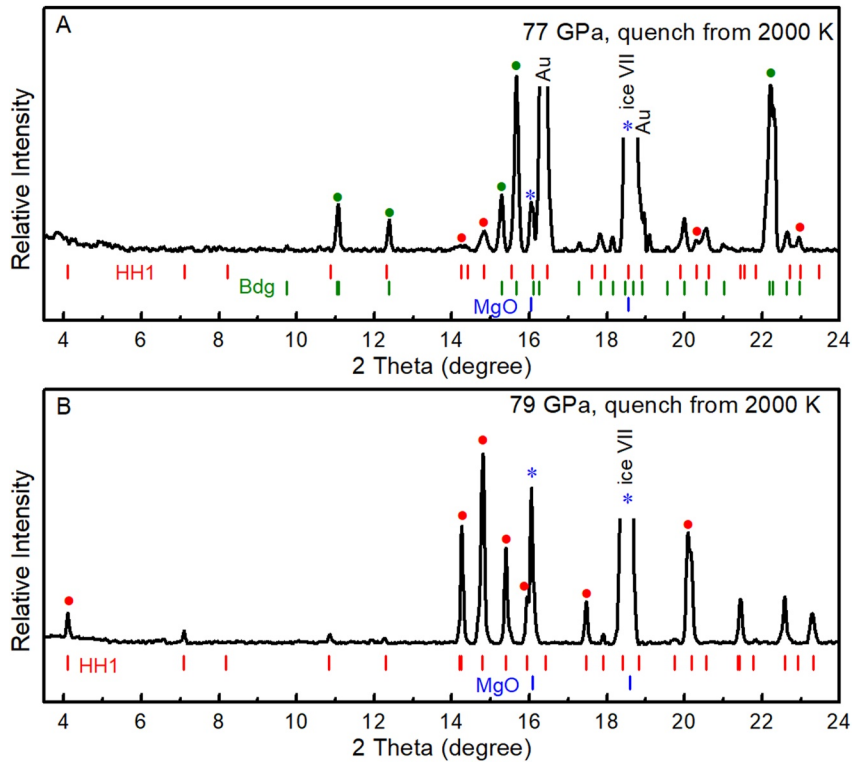

Figure 4. X-ray diffraction (XRD) patterns of the run products of the reactions: (a) natural olivine $[(Mg_{0.9}Fe_{0.1})_2SiO_4] + H_2O$ (b) $(Mg_{0.8}Fe_{0.2})O$ (Fp20) + H_2O under high *P-T* conditions of the deep lower mantle. The HH1-phase coexisted with Fp, and Bdg at 77 GPa and after *T* quench from 2000 K (Run# Sb329) in Figure 4a. The XRD peaks of HH1-phase are comparable to the peak (111) from the coexisting Fp-phase at 79 GPa and after *T* quench from 2000 K (Run# Sb430) in Figure 4b. The X-ray wavelength was 0.6199 Å.

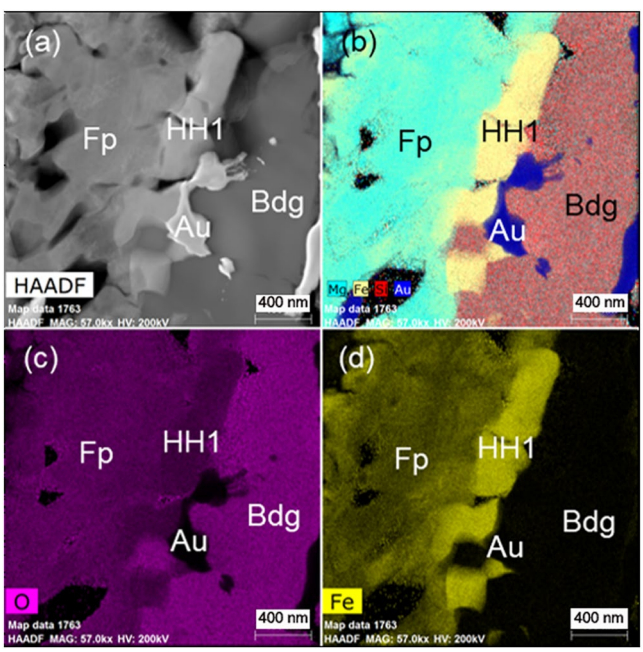

Figure 5. TEM images of the run product recovered from the reaction of olivine $[(Mg_{0.9}Fe_{0.1})_2SiO_4]$ and water 77 GPa and 2000 K, showing the coexistence of the HH1-phase with Fp and Bdg. Elemental mapping of Mg, Fe, Si, and O are shown in light blue, yellow, red, and purple, respectively (Run# Sb329).

4. Conclusions

Whether the HH1-phase plays a major role as water storage in the deep mantle largely depends on the chemical composition. The HH1-phase in the Fe-O-H system has a chemical formula of $Fe_{12.76}O_{18}H_x$ ($x \sim 4.5$), containing about 4.0 wt.% H_2O, but the chemical composition of the HH1-phase varies with bulk composition and with pressure. The stability of HH-phase in both MgO-rich and SiO_2-rich systems implies its ubiquitous existence in a wet deep lower mantle. Based on our experimental results, the Fp-phase can readily react with water to form the HH1-phase, making it a dominant water storage phase in a pyrolitic composition. The previous study suggested that seismic features in the LLSVPs can be best explained by material enriched in iron by ~3.0% and in (Mg,Fe)-Bdg by ~20% than a regular pyrolitic composition (Deschamps et al., 2012). In their model, the Fp-phase exceeds 8% in volume fraction and Fe preferentially partitions into the Fp-phase relative to Bdg throughout the entire lower mantle (Kobayashi et al., 2005), implying that the HH1-phase could play a major role for water storage in the LLSVPs. In contrast, the $CaCl_2$-type δ-phase and SiO_2 phase become major water reservoirs in regions where MORB accumulated but the HH1-phase still exists as an accessory phase. It has been suggested that the shear-wave velocity of high-pressure MORB is in contradiction with the observations in LLSVPs (Deschamps et al., 2012; Wang et al., 2020), but subduction and recycling of MORB might play an important role in deep mantle dynamics (Van der Hilst et al., 1997; Zhao, 2004).

Table 3
Chemical Compositions of the HH1-Phase With the Approximate Chemical Formula [(Mg,Si,Al, and Fe)]$_{12.76}O_{18}H_x$ (x ~ 4.5) Synthesized in the Multicomponent Systems[a]

Starting materials	MASFH30 (run# Sb335)	MASFH6 (run# Sb307b)	MASFH8 (run# Sb397)	$Al_{0.2}Fe_{0.8}(OH)_3$ (run# Sb343a)	Olivine + H_2O (run# Sb329)	Fp20 + H_2O (run# Sb430)
P	79 GPa	96 GPa	74 GPa	80 GPa	77 GPa	79 GPa
T	2000 K	2300 K	2000 K	2100 K	2000 K	2000 K
Mg (at%)	8.5 (1.7)	4.9 (1.3)	2.2 (1.6)		4.9 (0.8)	1.7 (0.3)
Si (at%)	11.2 (1.8)	12.6 (3.9)	11.9 (2.8)		7.1 (1.1)	
Al (at%)	1.4 (0.9)	11.2 (2.6)	2.3 (0.9)	1.5 (0.3)		
Fe (at%)	78.9 (2.4)	71.3 (5.9)	83.6 (5.1)	98.5 (0.3)	88.0 (1.7)	98.3 (0.3)

[a]The numbers in parenthesis are one standard deviation based on multiple analyses ($n \geq 3$).

The characteristics of seismically imaged plumes support the idea that hotspot volcanoes originate from hot upwelling rock rooted in the deepest mantle (French & Romanowicz, 2015). Such plumes might contain materials of lower viscosity than the bulk lower mantle. It has been known that the introduction of small amounts of water into the mantle system would greatly reduce its viscosity (Karato & Jung, 1998) and lower the melting temperature (Iwamori, 1998) as compared to that of the dry system. Therefore, our results of water storage and phase assemblages in mantle compositions might have significant implications for deep mantle dynamics. Unlike the Al-rich δ-phase that is stable throughout the entire lower mantle, the Fe-rich HH1-phase, if included into the material of upwelling plumes, will decompose on its rising to the upper part of the lower mantle and release water, thus affecting the dynamics of upwelling mantle plumes. In addition to the HH1-phase, several other phase transitions

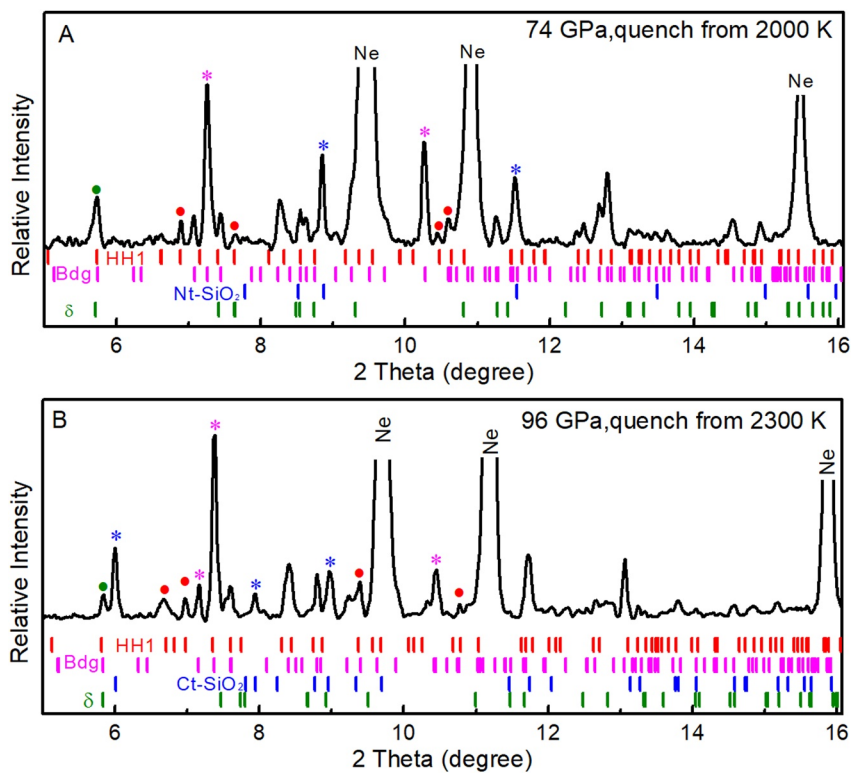

Figure 6. X-ray diffraction patterns of the run products in Mg-Si-Al-Fe-O-H systems under high *P-T* conditions of the deep lower mantle. (a) The HH1-phase coexisted with d-NiAs-type SiO_2, δ-phase, and bridgmanite 74 GPa and after *T* quench from 2000 K (Run# Sb397). The starting material was 54.8 mol % SiO_2-12.8 mol % Al_2O_3-24.9 mol % MgO-7.5 mol % Fe_2O_3+ ~7wt% H_2O (MASFH8) and the X-ray wavelength was 0.2904 Å. (b) The HH1-phase coexisted with $CaCl_2$-type SiO_2, δ-phase, and Bdg (Run# Sb307b). The starting material was MASFH6 (Table 1) and the X-ray wavelength was 0.2905 Å.

into hexagonal structures (Bykova et al., 2016; Zhang et al., 2014, 2018) have been found in Fe-bearing minerals under *P-T* conditions corresponding to the bottom half of the lower mantle. The lower mantle may consist of two physicochemically distinct zones separated at ~1,800 km depth and the property contrast at this boundary would provide fundamental driving forces in mantle dynamics (Mao & Mao, 2020). Future research is required to understand the combined effects of water and phase transitions on mantle dynamics in the deep lower mantle.

Data Availability Statement

The X-ray diffraction data sets of all Figures are available at (https://doi.org/10.5281/zenodo.6274869).

Acknowledgments
This work was supported from the National Natural Science Foundation of China (NSFC) (Grant No: 42150103). Portions of this work were performed at 15U1, Shanghai Synchrotron Radiation Facility. We acknowledge Deutsches Elektronen Synchrotron (Hamburg, Germany), a member of the Helmholtz Association HGF, for the provision of experimental facilities. Portions of this research were carried out at the P02.2 beamline of PETRA III. Portions of this work were performed at HPCAT (Sector 16), APS, Argonne National Laboratory. HPCAT operations are supported by the Department of Energy–National Nuclear Security Administration's (DOE-NNSA's) Office of Experimental Science. The Advanced Photon Source is a U.S. DOE Office of Science User Facility operated for the DOE Office of Science by Argonne National Laboratory under contract No. DE-AC02-06CH11357.

References

Akahama, Y., & Kawamura, H. (2007). Diamond anvil Raman gauge in multimegabar pressure range. *High Pressure Research*, *27*(4), 473–482. https://doi.org/10.1080/08957950701659544

Bengtson, A., Li, J., & Morgan, D. (2009). Mössbauer modeling to interpret the spin state of iron in (Mg,Fe)SiO_3 perovskite. *Geophysical Research Letters*, *36*(15), L15301. https://doi.org/10.1029/2009GL038340

Brown, J. M., & Shankland, T. J. (1981). Thermodynamic parameters in the Earth as determined from seismic profiles. *Geophysical Journal of the Royal Astronomical Society*, *66*(3), 579–596. https://doi.org/10.1111/j.1365-246x.1981.tb04891.x

Bykova, E., Dubrovinsky, L., Dubrovinskaia, N., Bykov, M., McCammon, C., Ovsyannikov, S. V., et al. (2016). Structural complexity of simple Fe_2O_3 at high pressures and temperatures. *Nature Communications*, *7*(1), 10661. https://doi.org/10.1038/ncomms10661

Chen, H., Xie, S. Y., Ko, B., Kim, T., Nisr, C., Prakapenka, V., et al. (2020). A new hydrous iron oxide phase stable at mid-mantle pressures. *Earth and Planetary Science Letters*, *550*, 116551. https://doi.org/10.1016/j.epsl.2020.116551

Deschamps, F., Cobden, L., & Tackley, P. J. (2012). The primitive nature of large low shear-wave velocity provinces. *Earth and Planetary Science Letters*, *349–350*, 198–208. https://doi.org/10.1016/j.epsl.2012.07.012

Dixon, J. E., Leist, L., Langmuir, C., & Schilling, J.-G. (2002). Recycled dehydrated lithosphere observed in plume-influenced mid-ocean-ridge basalt. *Nature*, *420*(6914), 385–389. https://doi.org/10.1038/nature01215

Fei, Y., Murphy, C., Shibazaki, Y., Shahar, A., & Huang, H. (2016). Thermal equation of state of hcp-iron: Constraint on the density deficit of Earth's solid inner core. *Geophysical Research Letters*, *43*(13), 6837–6843. https://doi.org/10.1002/2016GL069456

Fei, Y., Ricolleau, A., Frank, M., Mibe, K., Shen, G., & Prakapenka, V. (2007). Toward an internally consistent pressure scale. *Proceedings of the National Academy of Sciences*, *104*(22), 9182–9186. https://doi.org/10.1073/pnas.0609013104

Fischer, R. A., Campbell, A. J., Shofner, G. A., Lord, O. T., Dera, P., & Prakapenka, V. B. (2011). Equation of state and phase diagram of FeO. *Earth and Planetary Science Letters*, *304*(3), 496–502. https://doi.org/10.1016/j.epsl.2011.02.025

Foo, M. L., He, T., Huang, Q., Zandbergen, H. W., Siegrist, T., Lawes, G., et al. (2006). Synthesis and characterization of the pseudo-hexagonal hollandites $ALi_2Ru_6O_{12}$ (A=Na, K). *Journal of Solid State Chemistry*, *179*(3), 941–948. https://doi.org/10.1016/j.jssc.2005.12.011

French, S. W., & Romanowicz, B. (2015). Broad plumes rooted at the base of the Earth's mantle beneath major hotspots. *Nature*, *525*(7567), 95–99. https://doi.org/10.1038/nature14876

Fu, S., Yang, J., Karato, S., Vasiliev, A., Presniakov, M. Y., Gavriliuk, A. G., et al. (2019). Water concentration in single-crystal (Al, Fe)-bearing Bridgmanite grown from the hydrous melt: Implications for dehydration melting at the topmost lower mantle. *Geophysical Research Letters*, *46*(17–18), 10346–10357. https://doi.org/10.1029/2019GL084630

Gleason, A. E., Quiroga, C. E., Suzuki, A., Pentcheva, R., & Mao, W. L. (2013). Symmetrization driven spin transition in ε-FeOOH at high pressure. *Earth and Planetary Science Letters*, *379*, 49–55. https://doi.org/10.1016/j.epsl.2013.08.012

Greenberg, E., Xu, W. M., Nikolaevsky, M., Bykova, E., Garbarino, G., Glazyrin, K., et al. (2017). High-pressure magnetic, electronic, and structural properties of MFe_2O_4 (M = Mg, Zn, Fe) ferric spinels. *Physical Review B*, *95*(19), 195150. https://doi.org/10.1103/PhysRevB.95.195150

Holzapfel, C., Rubie David, C., Frost Daniel, J., & Langenhorst, F. (2005). Fe-Mg interdiffusion in (Mg, Fe)SiO_3 perovskite and lower mantle reequilibration. *Science*, *309*(5741), 1707–1710. https://doi.org/10.1126/science.1111895

Hu, Q., Kim, D. Y., Yang, W., Yang, L., Meng, Y., Zhang, L., & Mao, H.-K. (2016). FeO_2 and FeOOH under deep lower-mantle conditions and Earth's oxygen–hydrogen cycles. *Nature*, *534*(7606), 241–244. https://doi.org/10.1038/nature18018

Irifune, T., Shinmei, T., McCammon, C. A., Miyajima, N., Rubie, D. C., & Frost, D. J. (2010). Iron partitioning and density changes of pyrolite in Earth's lower mantle. *Science*, *327*(5962), 193–195. https://doi.org/10.1126/science.1181443

Iwamori, H. (1998). Transportation of H_2O and melting in subduction zones. *Earth and Planetary Science Letters*, *160*(1–2), 65–80. https://doi.org/10.1016/S0012-821X(98)00080-6

Jellinek, A. M., & Manga, M. (2002). The influence of a chemical boundary layer on the fixity, spacing and lifetime of mantle plumes. *Nature*, *418*(6899), 760–763. https://doi.org/10.1038/nature00979

Kabsch, W. (2010). XDS. *Acta Crystallographica Section D*, *66*(2), 125–132. https://doi.org/10.1107/S0907444909047337

Karato, S.-i., & Jung, H. (1998). Water, partial melting and the origin of the seismic low velocity and high attenuation zone in the upper mantle. *Earth and Planetary Science Letters*, *157*(3), 193–207. https://doi.org/10.1016/S0012-821X(98)00034-X

Katsura, T., Yoneda, A., Yamazaki, D., Yoshino, T., & Ito, E. (2010). Adiabatic temperature profile in the mantle. *Physics of the Earth and Planetary Interiors*, *183*(1), 212–218. https://doi.org/10.1016/j.pepi.2010.07.001

Kirby, S. H., Stein, S., Okal, E. A., & Rubie, D. C. (1996). Metastable mantle phase transformations and deep earthquakes in subducting oceanic lithosphere. *Reviews of Geophysics*, *34*(2), 261–306. https://doi.org/10.1029/96rg01050

Kobayashi, Y., Kondo, T., Ohtani, E., Hirao, N., Miyajima, N., Yagi, T., et al. (2005). Fe-Mg partitioning between (Mg, Fe)SiO_3 post-perovskite, perovskite, and magnesiowüstite in the Earth's lower mantle. *Geophysical Research Letters*, *32*(19), L19301. https://doi.org/10.1029/2005GL023257

Koemets, E., Fedotenko, T., Khandarkhaeva, S., Bykov, M., Bykova, E., Thielmann, M., et al. (2021). Chemical stability of FeOOH at high pressure and temperature, and oxygen recycling in early Earth history. *European Journal of Inorganic Chemistry*, *2021*(30), 3048–3053. https://doi.org/10.1002/ejic.202100274

Labrosse, S., Hernlund, J. W., & Coltice, N. (2007). A crystallizing dense magma ocean at the base of the Earth's mantle. *Nature*, *450*(7171), 866–869. https://doi.org/10.1038/nature06355

Litasov, K., Ohtani, E., Langenhorst, F., Yurimoto, H., Kubo, T., & Kondo, T. (2003). Water solubility in Mg-perovskites and water storage capacity in the lower mantle. *Earth and Planetary Science Letters*, *211*(1), 189–203. https://doi.org/10.1016/S0012-821X(03)00200-0

Liu, J., Wang, C., Lv, C., Su, X., Liu, Y., Tang, R., et al. (2020). Evidence for oxygenation of Fe-Mg oxides at mid-mantle conditions and the rise of deep oxygen. *National Science Review*, *8*(4), nwaa096. https://doi.org/10.1093/nsr/nwaa096

Liu, J., Xia, Q.-K., Kuritani, T., Hanski, E., & Yu, H.-R. (2017). Mantle hydration and the role of water in the generation of large igneous provinces. *Nature Communications*, *8*(1), 1824. https://doi.org/10.1038/s41467-017-01940-3

Mao, H.-K., Hu, Q., Yang, L., Liu, J., Kim, D. Y., Meng, Y., et al. (2017). When water meets iron at Earth's core–mantle boundary. *National Science Review*, *4*(6), 870–878. https://doi.org/10.1093/nsr/nwx109

Mao, H.-k., & Mao, W. L. (2020). Key problems of the four-dimensional Earth system. *Matter and Radiation at Extremes*, *5*(3), 038102. https://doi.org/10.1063/1.5139023

Maruyama, S., Santosh, M., & Zhao, D. (2007). Superplume, supercontinent, and post-perovskite: Mantle dynamics and anti-plate tectonics on the Core–Mantle Boundary. *Gondwana Research*, *11*(1), 7–37. https://doi.org/10.1016/j.gr.2006.06.003

Miura, H., Hamada, Y., Suzuki, T., Akaogi, M., Miyajima, N., & Fujino, K. (2000). Crystal structure of $CaMg_2Al_6O_{12}$, a new Al-rich high pressure form. *American Mineralogist*, *85*(11–12), 1799–1803. https://doi.org/10.2138/am-2000-11-1223

Nakagawa, T., Tackley, P. J., Deschamps, F., & Connolly, J. A. D. (2010). The influence of MORB and harzburgite composition on thermo-chemical mantle convection in a 3-D spherical shell with self-consistently calculated mineral physics. *Earth and Planetary Science Letters*, *296*(3), 403–412. https://doi.org/10.1016/j.epsl.2010.05.026

Ni, S., Tan, E., Gurnis, M., & Helmberger, D. (2002). Sharp sides to the African superplume. *Science*, *296*(5574), 1850–1852. https://doi.org/10.1126/science.1070698

Nishi, M., Irifune, T., Tsuchiya, J., Tange, Y., Nishihara, Y., Fujino, K., & Higo, Y. (2014). Stability of hydrous silicate at high pressures and water transport to the deep lower mantle. *Nature Geoscience*, *7*(3), 224–227. https://doi.org/10.1038/ngeo2074

Nishi, M., Kuwayama, Y., Tsuchiya, J., & Tsuchiya, T. (2017). The pyrite-type high-pressure form of FeOOH. *Nature*, *547*(7662), 205–208. https://doi.org/10.1038/nature22823

Nisr, C., Chen, H., Leinenweber, K., Chizmeshya, A., Prakapenka, V. B., Prescher, C., et al. (2020). Large H_2O solubility in dense silica and its implications for the interiors of water-rich planets. *Proceedings of the National Academy of Sciences*, *117*(18), 9747–9754. https://doi.org/10.1073/pnas.1917448117

Ohira, I., Ohtani, E., Sakai, T., Miyahara, M., Hirao, N., Ohishi, Y., & Nishijima, M. (2014). Stability of a hydrous δ-phase, AlOOH–$MgSiO_2$(OH) 2, and a mechanism for water transport into the base of lower mantle. *Earth and Planetary Science Letters*, *401*, 12–17. https://doi.org/10.1016/j.epsl.2014.05.059

Pamato, M. G., Myhill, R., Boffa Ballaran, T., Frost, D. J., Heidelbach, F., & Miyajima, N. (2015). Lower-mantle water reservoir implied by the extreme stability of a hydrous aluminosilicate. *Nature Geoscience*, *8*(1), 75–79. https://doi.org/10.1038/ngeo2306

Pépin, C. M., Dewaele, A., Geneste, G., Loubeyre, P., & Mezouar, M. (2014). New iron hydrides under high pressure. *Physical Review Letters*, *113*(26), 265504. https://doi.org/10.1103/PhysRevLett.113.265504

Prakapenka, V. P., Shen, G., Dubrovinsky, L. S., Rivers, M. L., & Sutton, S. R. (2004). High pressure induced phase transformation of SiO_2 and GeO_2: Difference and similarity. *Journal of Physics and Chemistry of Solids*, *65*(8), 1537–1545. https://doi.org/10.1016/j.jpcs.2003.12.019

Ricolleau, A., Fei, Y., Cottrell, E., Watson, H., Deng, L., Zhang, L., et al. (2009). Density profile of pyrolite under the lower mantle conditions. *Geophysical Research Letters*, *36*(6), L06302. https://doi.org/10.1029/2008GL036759

Sano, A., Ohtani, E., Kondo, T., Hirao, N., Sakai, T., Sata, N., et al. (2008). Aluminous hydrous mineral δ-AlOOH as a carrier of hydrogen into the core-mantle boundary. *Geophysical Research Letters*, *35*(3), L03303. https://doi.org/10.1029/2007GL031718

Schmidt, S. (2014). GrainSpotter: A fast and robust polycrystalline indexing algorithm. *Journal of Applied Crystallography*, *47*(1), 276–284. https://doi.org/10.1107/S1600576713030185

Sobolev, A. V., Asafov, E. V., Gurenko, A. A., Arndt, N. T., Batanova, V. G., Portnyagin, M. V., et al. (2016). Komatiites reveal a hydrous Archaean deep-mantle reservoir. *Nature*, *531*(7596), 628–632. https://doi.org/10.1038/nature17152

Sørensen, H. O., Schmidt, S., Wright, J. P., Vaughan, G. B. M., Techert, S., Garman, E. F., et al. (2012). Multigrain crystallography. *Zeitschrift für Kristallographie*, *227*(1), 63–78. https://doi.org/10.1524/zkri.2012.1438

Su, W.-j., Woodward, R. L., & Dziewonski, A. M. (1994). Degree 12 model of shear velocity heterogeneity in the mantle. *Journal of Geophysical Research*, *99*(B4), 6945–6980. https://doi.org/10.1029/93JB03408

Thorne, M. S., Garnero, E. J., & Grand, S. P. (2004). Geographic correlation between hot spots and deep mantle lateral shear-wave velocity gradients. *Physics of the Earth and Planetary Interiors*, *146*(1), 47–63. https://doi.org/10.1016/j.pepi.2003.09.026

Trampert, J., Deschamps, F., Resovsky, J., & Yuen, D. (2004). Probabilistic tomography maps chemical heterogeneities throughout the lower mantle. *Science*, *306*(5697), 853–856. https://doi.org/10.1126/science.1101996

Van der Hilst, R. D., Widiyantoro, S., & Engdahl, E. (1997). Evidence for deep mantle circulation from global tomography. *Nature*, *386*(6625), 578–584. https://doi.org/10.1038/386578a0

Walter, M. J., Thomson, A. R., Wang, W., Lord, O. T., Ross, J., McMahon, S. C., et al. (2015). The stability of hydrous silicates in Earth's lower mantle: Experimental constraints from the systems MgO–SiO_2–H_2O and MgO–Al_2O_3–SiO_2–H_2O. *Chemical Geology*, *418*, 16–29. https://doi.org/10.1016/j.chemgeo.2015.05.001

Wang, W., Xu, Y., Sun, D., Ni, S., Wentzcovitch, R., & Wu, Z. (2020). Velocity and density characteristics of subducted oceanic crust and the origin of lower-mantle heterogeneities. *Nature Communications*, *11*(1), 1–8. https://doi.org/10.1038/s41467-019-13720-2

Yuan, H., Zhang, L., Ohtani, E., Meng, Y., Greenberg, E., & Prakapenka, V. B. (2019). Stability of Fe-bearing hydrous phases and element partitioning in the system MgO–Al_2O_3–Fe_2O_3–SiO_2–H_2O in Earth's lowermost mantle. *Earth and Planetary Science Letters*, *524*, 115714. https://doi.org/10.1016/j.epsl.2019.115714

Zhang, L., Meng, Y., Yang, W., Wang, L., Mao, W. L., Zeng, Q. S., et al. (2014). Disproportionation of (Mg, Fe)SiO(3) perovskite in Earth's deep lower mantle. *Science*, *344*(6186), 877–882. https://doi.org/10.1126/science.1250274

Zhang, L., Popov, D., Meng, Y., Wang, J., Ji, C., Li, B., & Mao, H.-k. (2016). In-situ crystal structure determination of seifertite SiO_2 at 129 GPa: Studying a minor phase near Earth's core–mantle boundary. *American Mineralogist*, *101*(1), 231–234. https://doi.org/10.2138/am-2016-5525

Zhang, L., Yuan, H., Meng, Y., & Mao, H.-k. (2018). Discovery of a hexagonal ultradense hydrous phase in (Fe, Al)OOH. *Proceedings of the National Academy of Sciences*, *115*(12), 2908–2911. https://doi.org/10.1073/pnas.1720510115

Zhang, L., Yuan, H., Meng, Y., & Mao, H.-K. (2019). Development of high-pressure multigrain X-ray diffraction for exploring the Earth's interior. *Engineering*, *5*(3), 441–447. https://doi.org/10.1016/j.eng.2019.02.004

Zhao, D. (2004). Global tomographic images of mantle plumes and subducting slabs: Insight into deep Earth dynamics. *Physics of the Earth and Planetary Interiors*, *146*(1), 3–34. https://doi.org/10.1016/j.pepi.2003.07.032